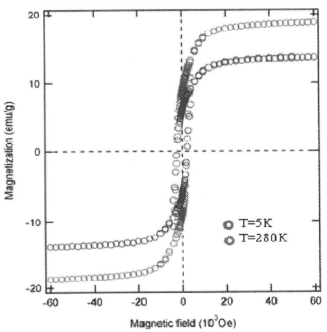

Figure 5. Hysteresis loops at room temperature of the Ba-hexaferrite nanocrystals synthesized with oleic acid capping.

factors. Possibly, the large surface area of the particles and the incomplete coordination of atoms at the particle surface lead to a noncollinear spin configuration. Consequently, significant reduction of the magnetization emerges with increase in the surface volume ratio of small particles. Therefore, coercivity, H_c, of small particles increases by decreasing the particle size. In the present study, coercivity of organic ligand capped nanocrystals is 2800 Oe and this is higher than that of the nanodisc[14] and comparable with the nanoparticles synthesized by other methods.[17] Further study is carried out to improve the magnetic properties of the Ba-hexaferrite nanocrystals and will be reported in our next communications.

Formation Mechanism. The formation and growth mechanism of the Ba-hexaferrite nanocrystals can be attributed to the kinetic effect, which determines the final size and morphology of the nanocrystals. The formation of Ba-hexaferrite colloidal nanocrystals takes place in three stages; at first, sub-10 nm single nanocrystals were formed at mixing point, when the precursor solution was mixed with a supercritical water; second, organic molecules miscible with the high temperature water; and finally, the controlled growth of the nanocrystal occurs by the selective reaction of organic molecules with the specific inorganic crystal surface.

The successful synthesis of the monodisperse nanocrystals can be attributed to the higher degree of supersaturation and effective control of the growth process under the organic ligand assisted SCW conditions. Park et al.[6] reported the synthesis of monodisperse metal oxide nanocrystals by the separation of nucleation and growth processes. Drofenik et al.[14] employed the LaMer-dinger principle to synthesize the monodisperse Ba-hexaferrite nanoparticles through controlled hydrothermal synthesis. These reports indicate that the separation of nucleation and crystal growth processes would facilitate the formation of monodisperse nanocrystal. In the SCW synthesis, a high reaction rate and lower solubility for the formed metal oxide can be achieved above the critical temperature of water. This causes an extremely high degree of supersaturation of the metal oxide and thus allows the nanoparticle formation at the mixing point, MP1, where the temperature was 450−500 °C. With the addition of organic molecules into the reaction system at the mixing point, MP2 with the set up temperature 350−380 °C (Figure 1), the organic molecules were miscible with water under supercritical condition due to the lower dielectric constant of SCW. This provides a homogeneous reaction medium with suitable environment for the selective interaction between the organic ligand and the nanocrystal surface, when oleic acid

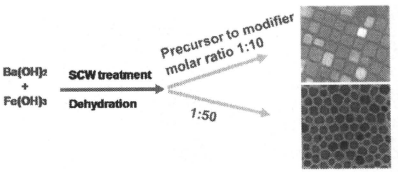

Figure 6. Schematic representation of Ba-hexaferrite nanocrystals size and morphology control under different surfactant ratios under supercritical water conditions.

concentration was about 10:1 molar ratio to Ba-hexaferrite. The selective absorption of the organic ligand onto the reactive face of nanocrystal occurs during the growth process, which results in the nano cube shape particle formation as displayed in the reaction mechanism diagram (Figure 6). By increasing the oleic acid reagent concentration above 50:1 molar ratio (to Ba-hexaferrite) the organic molecules covered all the faces of Ba-hexaferrite and inhibited the inhomogeneous growth of the nuclei resulting in the octahedron shaped nanocrystals. These results suggest that the selective adsorption of the organic ligand can effectively inhibit the growth of the favorable crystallographic planes of the nanocrystals.[6] Zhang et al.[9] reported that the shape transformation of ceria nanocrystals from cubic to truncated octahedron was mostly caused by the suppression of the crystal growth on the [001] surface under similar organic ligand assisted SCW conditions with an increase in the organic ligand concentration. Radwan et al. reported the effect of anionic, cationic, and nonionic surfactants on the microstructures of Ba-hexaferrite nanoparticles of sub-micrometer size through the coprecipitation−calcination route.[13b]

The organic molecules are stable at supercritical water conditions as the time constants for the decomposition of organic molecules at 400 °C is on the order of 10−30 min without oxidizing agents. Watanabe et al.[15] and Savage[16] have reported the decomposition reactions of different organic materials at supercritical state.

Conclusion. In conclusion, we have successfully synthesized the shape- and size-controlled Ba-hexaferrite nanocrystals capped with oleic acid ligand under supercritical water hydrothermal conditions. The results showed that the concentration of oleic acid reagent in the starting precursor is a key to control the cubic and octahedral shape of Ba-hexaferrite nanocrystals. This indicates that the size and morphology of nanocrystals were greatly influenced by the organic ligand capping resulting in the drastic reduction of the particle size from 28 to 9 nm. The organic modified Ba-hexaferrite nanocrystals magnetic property is consistent with the magnetic state of Ba-hexaferrite nanoparticles reported in the literature.

References

(1) (a) Fujiwara, T. *IEEE Trans. Magn.* **1985**, *21*, 1480. (b) Penkov, V. V.; Pernet, M.; Germi, P.; Mollard, P. *J. Magn. Magn. Mater.* **1993**, *120*, 69.
(2) Bregar, V. B. *IEEE Trans. Magn.* **2004**, *40*, 1679.
(3) (a) Tateno, Y. *J. Appl. Phys.* **2002**, *91*, 4418. (b) Rezlescu, E.; Rezlescu, L.; Popa, P. D.; Rezlescu, N. *Mater. Sci. Eng., A* **2004**, *375−377*, 1269.
(4) (a) Lui, X.; Wang, J.; Gan, L.-M.; Ng, S.-C.; Ding, J. *J. Magn. Magn. Mater.* **1998**, *184*, 344. (b) Jacobo, S. E.; Domingo-Pascal, C.; Rodriguez-Clemente, R.; Blesa, M. A. *J. Mater. Sci.* **1997**, *32*, 1025. (c) Muller, R.; Heirgeist, R.; Steinmetz, H.; Ayoub, N.; Fujisaki, M.; Schuppel, W. *J. Magn. Magn. Mater.* **1999**, *201*, 34. (d) Huang, J.; Zhuang, H.; Li, W. *Mater. Res. Bull.* **2003**, *38*, 149. (e) Sudakar, C.;

Subbanna, G. N.; Kutty, T. R. N. *J. Magn. Magn. Mater.* **2003**, *263*, 253.
(5) Hakuta, Y.; Adschiri, T.; Suzuki, T.; Chida, T.; Seino, K.; Arai, K. *J. Am. Ceram. Soc.* **1998**, *81*, 2461.
(6) Park, J.; An, K.; Hwang, Y.; Park, J. G.; Noh, H. J.; Kim, J. Y.; Park, J. H.; Hwang, N. M.; Hyeon, T. *Nat. Mater.* **2004**, *3*, 891.
(7) Hyeon, T.; Lee, S. S.; Park, J.; Chung, Y.; Na, H. B. *J. Am. Chem. Soc.* **2001**, *123*, 12798.
(8) (a) Adschiri, T. *Chem. Let.* **2007**, *36*, 1188. (b) Adschiri, T.; Hakuta, Y.; Arai, K. *Ind. Eng. Chem. Res.* **2000**, *39*, 4901. (c) Adschiri, T.; Kanazawa, K.; Arai, K. *J. Am. Ceram. Soc.* **1992**, *75*, 1019.
(9) (a) Zhang, J.; Ohara, S.; Umetsu, M.; Naka, T.; Hatakeyama, Y.; Adschiri, T. *Adv. Mater.* **2007**, *19*, 203. (b) Mousavand, T.; Takami, S.; Ohara, S.; Umetsu, M.; Adschiri, T. *J. Nanosci. Nanotechnol.* **2005**, *1*, 85.
(10) (a) Mousavand, T.; Takami, S.; Ohara, S.; Umetsu, M.; Adschiri, T. *J. Supercrit. Fluids* **2007**, *40*, 397. (b) Devaraju, M. K.; Yin, S.; Sato, T. *Cryst. Growth Des.* **2009**, *9* (6), 2944.
(11) (a) Ziegler, K. J.; Doty, R. C.; Johnston, K. P.; Korgel, B. A. *J. Am. Ceram. Soc.* **2001**, *123*, 7797. (b) Mousavand, T.; Takami, S.; Ohara, S.; Umetsu, M.; Adschiri, T. *J. Mater. Sci.* **2006**, *41*, 1445.
(12) (a) Rangappa, D.; Ohara, S.; Naka, T.; Kondo, A.; Ishii, M.; Adschiri, T. *J. Mater. Chem.* **2007**, *129* (36), 11066. (b) Rangappa, D.; Naka, T.; Kondo, A.; Ishii, M.; Kobayashi, T; Adschiri, T. *J. Am. Chem. Soc.* **2007**, *129* (36), 11066.
(13) (a) Primc, D.; Makovec, D.; Lisjak, D.; Drofenik, M. *Nantotechnology* **2009**, *20*, 315605. (b) Radwan, M.; Rashad, M. M.; Hessien, M. M. *J. Mater. Pro. Tech.* **2007**, *181*, 106.
(14) Drofenik, M.; Kristl, M. *J. Am. Ceram. Soc.* **2007**, *90*, 2057.
(15) Watanabe, M.; Tsukagoshi, M.; Hirakoso, H.; Adschiri, T.; Arai, K. *AIChE J.* **2000**, *46*, 843.
(16) Savage, P. E. *Chem. Rev.* **1999**, *99*, 603.
(17) (a) Gonzalez., C, T.; Morales, M. P.; Serna, C. J. *Mater. Lett.* **2000**, *43*, 97. (b) Zhong, W.; Ding, W. P.; Zhang, N.; Hong, J. M.; Yan, A. J.; Du, Y. W. *J. Magn. Magn. Mater* **1997**, *168*, 196.

ORIGINAL RESEARCH PAPER

Fuel Cells DOI: 10.1002/fuce.200900095

Fine-microstructure Mediated Efficient Hydrogen Oxidation in Ni/YSZ Anode Fabricated from Novel Co-precipitation Derived Nanocomposites

K. Sato[1]*, T. Kinoshita[2], and H. Abe[1]

[1] Joining and Welding Research Institute, Osaka University, 11-1 Mihogaoka, Ibaraki, Osaka 567-0047 Japan
[2] New Technology Research Laboratory, Sumitomo Osaka Cement Co., Ltd, 585 Toyotomi-Cho, Funabashi, Chiba 247-8601, Japan

Received May 01, 2009; accepted December 25, 2009

Abstract

Fine-microstructure mediated efficient hydrogen oxidation was demonstrated on nickel/yttria-stabilised zirconia (Ni/YSZ) anode fabricated from NiO/YSZ nanocomposite particles, synthesised *via* a novel co-precipitation method using YSZ nanoparticles with the average size of 3 nm. Transmission electron microscopy image revealed that nanocomposite particles calcined at 600 °C consisted of homogeneously distributed NiO and YSZ nanocrystals, approximately 5 nm large. The Ni/YSZ anode was fabricated by sintering the screen-printed nanocomposites at 1,300 °C and their subsequent reduction. The anode had a uniform porous microstructure consisting of fine grains in the range of 200–300 nm, and exhibited quite low area-specific resistance (ASR) of 2.29, 0.43 and 0.15 Ω cm^2 at 600, 700 and 800 °C, respectively.

Keywords: AC-Impedance Spectroscopy, Co-precipitation, Nanoscopic Colloids; NiO/YSZ Nanocomposites, Ni/YSZ Anode, Performance Improvement, Solid Oxide Fuel Cell

1 Introduction

Nickel/yttria-stabilised zirconia (Ni/YSZ) cermet is a promising anode material for solid oxide fuel cells (SOFCs). Fundamental studies using well-defined model Ni anode on YSZ electrolyte revealed that hydrogen is oxidised in the vicinity of the triple phase boundary (TPB) where Ni, YSZ and pore phases meet [1, 2]. Considerable efforts in performance enhancement have been directed to enlarge the TPB within the limited effective electrode volume by controlling the microstructure [3–8].

Recent detailed electrochemical investigations suggested that the dominant rate-limiting steps of hydrogen oxidation are dissociative adsorption of hydrogen molecules, surface diffusion of adsorbed hydrogen atoms to the TPB and hydrogen oxidation at the TPB in the high performance Ni/YSZ cermet anode [9, 10]. Contribution of these steps must be reduced for further enhancement of hydrogen oxidation. Anodes with finer microstructure, consisting of homogeneously arranged as well as three-dimensionally percolating Ni, YSZ and pore phases, are promising candidates for the efficient hydrogen oxidation.

It has been demonstrated that the prefabrication of NiO/YSZ composite particles and their three-dimensional assembly using conventional ceramics processing is an effective way for accurately arranging the three phases [5, 6, 11–14]. Furthermore, co-existing NiO and YSZ can suppress each other's grain growth during sintering [6, 14]. Therefore, the synthesis of nano-sized NiO/YSZ composite particles is a promising route for achieving superior hydrogen oxidation characteristics of the Ni/YSZ anode.

In the present study, we have developed a novel co-precipitation method using aqueous suspension of YSZ nanoparticles for the synthesis of NiO/YSZ nanocomposite particles.

[*] *Corresponding author, k-sato@jwri.osaka-u.ac.jp*

The specific features of the YSZ nanoparticles were their small size (3 nm in diameter) and superior dispersion properties (almost no agglomeration) in an aqueous medium. In the present method, non-crystalline nickel carbonate hydroxide ($Ni(CO_3)_{2/3}(OH)_{2/3}{\cdot}nH_2O$) was nucleated onto the surface of dispersed YSZ nanoparticles, and the two were precipitated simultaneously. Thus, nanocomposite particles consisting of homogeneously distributed NiO and YSZ nanoparticles were obtained after the calcination. The resulting Ni/YSZ anode, consisting of fine grains in the range 200–300 nm, showed hydrogen oxidation superior to that reported in the literatures [3, 10, 15–17].

2 Experimental Procedure

2.1 Synthesis of NiO/YSZ Nanocomposite Particles

An aqueous suspension of YSZ nanoparticles (Sumitomo Osaka Cement Co. Ltd., Japan) shown in Figure 1(a) was used as the starting material. Dynamic light scattering method revealed that the suspension contained tiny nanoparticles (average diameter 3 nm) with a narrow size distribution (Figure 1(b)). The size determined *via* the light scattering method was in good agreement with that observed by transmission electron microscopy (TEM) (Figure 1 (c)). This agreement indicated that the 3-nm YSZ nanoparticles were well dispersed, without forming large agglomerates in the aqueous medium, resulting in the highly transparent appearance of the suspension due to significantly suppressed visible light scattering.

The suspension was mixed with a $Ni(NO_3)_2{\cdot}6H_2O$ (Kanto chemicals, Japan) aqueous solution. The amount of $Ni(NO_3)_2{\cdot}6H_2O$ was controlled as the volume fraction of Ni in the final anode to be 0.5. Total concentrations of YSZ and $Ni(NO_3)_2{\cdot}6H_2O$ were 0.2 M. Even after mixing, the solution maintained a high degree of transparency, indicating that the YSZ nanoparticles preserved their well dispersed state. The solution was added dropwise into 0.4 M of NH_4HCO_3 (Kanto chemicals, Japan) aqueous solution to nucleate $Ni(CO_3)_{2/3}(OH)_{2/3}{\cdot}nH_2O$ onto the surface of YSZ nanoparticles, and to precipitate them simultaneously as the precursor of the NiO/YSZ nanocomposite particles. During the co-precipitation, NH_3 solution (Wako chemicals, Japan) was added simultaneously into NH_4HCO_3 solution to keep the pH at 8. The precursor was rinsed and then dried in an oven at 80 °C for 24 h. Finally, the NiO/YSZ nanocomposite particles were obtained by calcining the dried precursor above 600 °C.

Phase identification of the precursor and of the composite particles was carried out using powder X-ray diffraction (XRD, JDX-3530M, JEOL, Japan) using Cu-ka radiation (λ = 0.1542 nm) as the X-ray source. Microstructure was observed by TEM (JEM-2100F, JEOL, Japan).

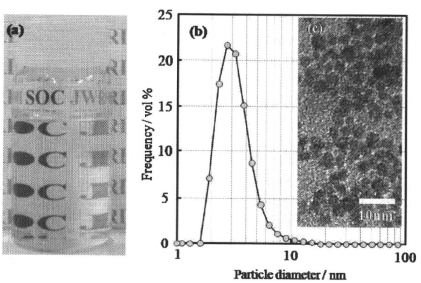

Fig. 1 (a) Optical appearance of aqueous suspension of YSZ nanoparticles, (b) Size distribution of the YSZ nanoparticles in the aqueous medium examined by dynamic light scattering and (c) TEM image of the YSZ nanoparticles.

2.2 Cell Fabrication and Electrochemical Performance Testing

An electrolyte-supported cell was employed for electrochemical performance testing. Firstly, fully dense YSZ electrolyte with the thickness of 300 μm and the diameter of 13 mm was fabricated by conventional tape casting, followed by sintering at 1,350 °C for 2 h. Then the anode was fabricated on top of the electrolyte by screen printing a paste of NiO/YSZ nanocomposite particles calcined at 1,000 °C and polyethylene glycol, followed by sintering at 1,300 °C for 2 h. Finally, the cathode was fabricated by screen printing of the $La_{0.8}Sr_{0.2}MnO_3$ paste and subsequent sintering at 1,100 °C for 2 h [18].

Three electrode-four lead configuration was used as the testing geometry. The cell was fixed between alumina tubes with a glass sealant. A Pt mesh connected with Pt wires was placed on both the anode and the cathode as a current collector. A Pt wire was attached along the circumference of the electrolyte as a reference electrode. Pt paste was applied to the reference electrode to improve electrical contact. The cell was heated to 900 °C to soften the glass sealant for gas tightening. During this process, nitrogen was supplied to the anode, and dry air was supplied to the cathode and the reference electrode with a flow rate of 0.05 l min^{-1}. After the temperature was reduced to 800 °C, anode gas atmosphere was altered from nitrogen to 3% humidified hydrogen with the flow rate of 0.05 l min^{-1}. At this stage NiO was reduced *in situ* into Ni, forming pores in the microstructure. Hydrogen oxidation of the Ni/YSZ anode was examined by area-specific resistance (ASR) measured with electrochemical impedance spectroscopy (EIS) at 600, 700 and 800 °C. The EIS spectra were recorded using a frequency response analyser with a potentiostat (Parstat 2263, Princeton Applied Research, TN) in the frequency range 0.1–10^5 Hz, under open circuit voltage (OCV) with an applied amplitude of 20 mV, after the ASR became constant (approximately 1 h from the starting of the test). The anode microstructure was observed by scanning electron microscopy (SEM, ERA-8800FE, Elionics, Japan).

3 Results and Discussion

Figure 2 shows the XRD pattern and a high resolution TEM (HRTEM) image of the precursor. Only the peaks corresponding to YSZ were observed in the XRD pattern. This indicates that non-crystalline $Ni(CO_3)_{2/3}(OH)_{2/3}{\cdot}nH_2O$ was present. The HRTEM image revealed that the crystalline YSZ nanoparticles (in the circles) were uniformly distributed throughout the entire non-crystalline $Ni(CO_3)_{2/3}(OH)_{2/3}{\cdot}nH_2O$ phase. This result suggests that $Ni(CO_3)_{2/3}(OH)_{2/3}{\cdot}nH_2O$ phase preferentially nucleated onto the YSZ surfaces.

Figure 3 shows the XRD pattern and a HRTEM image of the NiO/YSZ nanocomposite particles after calcination at 600 °C. The peaks of both the YSZ and the NiO phases were observed in the XRD pattern. The average crystalline size of NiO and YSZ phases, estimated by Scherrer's formula using full width at half maxima (FWHM) on NiO(200) (2θ = 43.30°) and YSZ (111) (2θ = 30.06°) peaks, was about 6 and 4 nm, respectively. The HRTEM image evidenced successful fabrication of the NiO/YSZ nanocomposite particles with the size of about 5 nm. This good agreement in crystalline sizes estimated from the XRD pattern with that examined on the HRTEM image indicated that the peak broadening in the XRD pattern was attributed to a small crystalline size rather than some micro-strain of the crystal lattices.

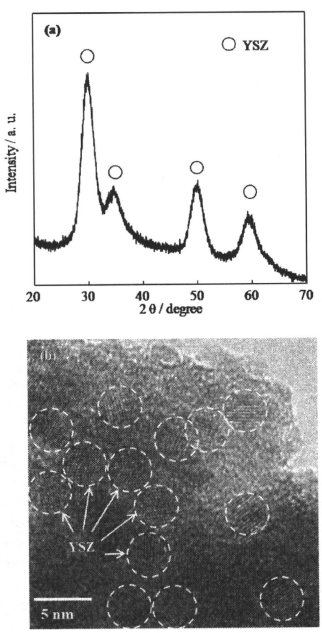

Fig. 2 (a) XRD pattern and (b) HRTEM image of the precipitated precursor.

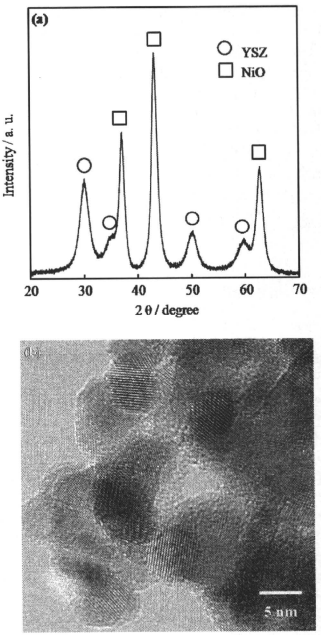

Fig. 3 (a) XRD pattern and (b) HRTEM image of the NiO/YSZ nanocomposite particles calcined at 600 °C.

It was reported that NiO nanoparticles synthesised in a similar manner could grow up to 13 nm in diameter, even though the precursor was calcined at 400 °C [19]. The size of NiO nanoparticles in the nanocomposite was less than a half of them. This fact indicated that homogeneously distributed YSZ nanoparticles within the precursor, as shown in Figure 2, significantly retarded the grain growth of NiO during the calcination.

Figure 4 shows SEM images of the Ni/YSZ anode after electrochemical performance testing. The low magnification image shows that the anode has uniform as well as fine porous microstructure. The high magnification image reveals that the anode consisted of fine grains in the range of 200–300 nm. Fine and well percolating solid and pore phases can be attributed to the homogeneous arrangement of NiO and YSZ phases in the nanocomposite particles. Grain size is one order of magnitude smaller than that of conventional anodes. The porosity of the anode estimated from the pore

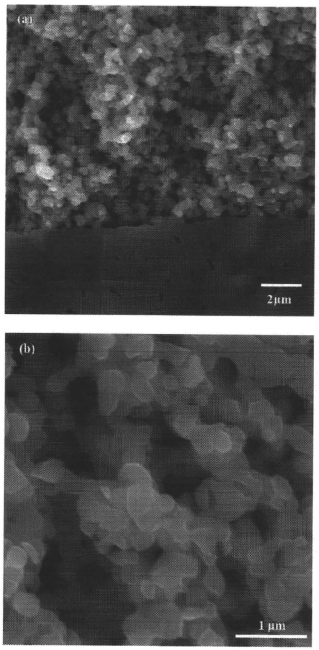

Fig. 4 (a) Low and (b) high magnification SEM images of the Ni/YSZ anode after the electrochemical performance testing.

area in a TEM image for the thin section (not shown here) was approximately 30% which is similar to that of the conventional anode [18].

Figure 5 shows EIS spectra of the anode. The ohmic resistance was subtracted from the total impedance for easier read out of ASR for the hydrogen oxidation [15]. ASR of the anode was 2.29, 0.43 and 0.15 Ω cm^2 at 600, 700 and 800 °C, respectively. These values were significantly lower than those reported in the literatures on Ni/YSZ anodes [3, 10, 12–17]. It has been proposed that the impedance semicircle could be divided into high frequency (1 k–50 kHz) [20, 21], medium frequency (10–1 kHz) [15] and low frequency (0.1–10 Hz) arcs [22]. The high frequency arc is reported to be responsible for the microstructure related processes involving gas–solid (desorption, adsorption and dissociation) [20] or solid–solid reactions (surface diffusion and electrochemical hydrogen oxidation at the TPB) [21]. These reactions are the main rate-limiting steps in a high-performance anode [9, 10]. A considerably smaller high frequency arc indicates highly efficient transport and electrochemical oxidation of hydrogen in the

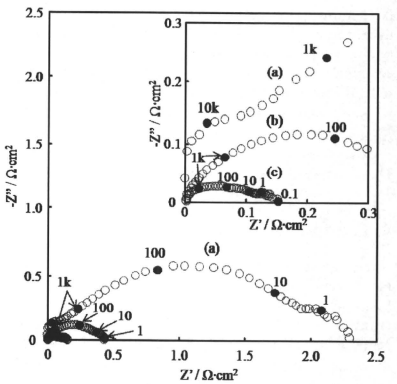

Fig. 5 EIS spectra of the anode measured at (a) 600, (b) 700 and (c) 800 °C under OCV.

present anode. It is clearly attributable to the fine microstructure shown in Figure 4, leading to extended adsorption sites and reduced diffusion length of hydrogen, in addition to the significantly enlarged TPB.

Figure 6 summarises the Arrhenius plot for polarisation resistance of the present Ni/YSZ anode and those of Ni/YSZ [3, 10, 15–17], CeO_2 doped Ni/YSZ [8] and Ni/Gd doped CeO_2 (GDC) [23] anodes with a YSZ electrolyte reported in the literatures. The activation energy is estimated to be 1.2 eV, which is similar to literature values for the Ni/YSZ anodes [15–17]. Although the activation energy is higher than CeO_2-doped Ni/YSZ [8] and Ni/ GDC [23] anodes, which

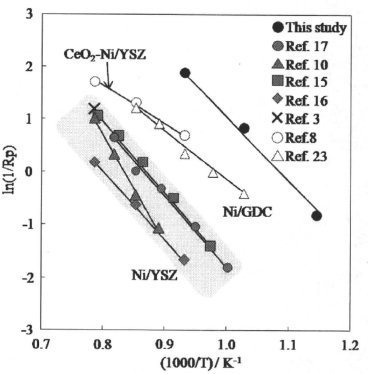

Fig. 6 Arrhenius plots of ASR of the Ni/YSZ anode in comparison with those of Ni/YSZ, CeO_2-Ni/YSZ and Ni/GDC anodes from the literatures.

have intrinsically higher catalytic activity than Ni/YSZ, the hydrogen oxidation characteristics of our anode are higher than those of anodes above 700 °C, and are expected to be comparable even at 600 °C. This result implies that the most reliable YSZ electrolyte and Ni/YSZ anode configuration can be used for lower temperature SOFC.

The durability of the microstructure and the performance of this fine grained Ni/YSZ anode are very important topic. This will be reported in the future work.

4 Conclusion

We have demonstrated that NiO/YSZ nanocomposite particles synthesised *via* a novel co-precipitation method with YSZ nanoparticles can provide fine, uniform porous microstructure of the Ni/YSZ anode. The anode exhibited significantly more efficient hydrogen oxidation compared to those in the literature. The superior performance can be attributed to finer-microstructure mediated rapid transport and oxidation of hydrogen. This new approach has great potential for application in a variety of composites for further performance enhancement of the SOFC.

Acknowledgement

This study was partially supported by the Industrial Technology Research Grant Program from the New Energy and Industrial Technology Development Organisation (NEDO) of Japan. This study was also supported by the Kansai Research Foundation for Technology Promotion.

References

[1] J. Mizusaki, H. Tagawa, T. Saito, K. Kamitani, T. Takagi, T. Hikita, M. Ippommatsu, S. Nakagawa, K. Hasgimoto, *J. Electrochem. Soc.* **1994**, *141*, 2129.

[2] A. Bieberle, L. P. Meier, L. J. Gauckler, *J. Electrochem. Soc.* **2001**, *148*, A646.

[3] T. Kawada, N. Sakai, H. Yokokawa, M. Dokiya, M. Mori, T. Iwata, *J. Electrochem. Soc.* **1990**, *137*, 3042.

[4] S.-D. Kim, H. Moon, S.-H. Hyun, J. Moon, J. Kim, H.-W. Lee, *J. Power Sources* **2006**, *163*, 392

[5] T. Fukui, S. Ohara, M. Naito, K. Nogi, *J. Power Sources* **2002**, *110*, 91.

[6] T. Fukui, K. Murata, S. Ohara, H. Abe, M. Naito, K. Nogi, *J. Power Sources* **2004**, *125*, 17.

[7] S. P. Jiang, S. Zhang, Y. D. Zhen, W. Wang, *J. Am. Ceram. Soc.* **2005**, *88*, 1779.

[8] S. P. Jiang, Y. Y. Duan, J. G. Love, *J. Electrochem. Soc.* **2002**, *149*, A1175.

[9] S. P. Jiang, S. P. S. Badwal, *J. Electrochem. Soc.* **1997**, *144*, 3777.

[10] S. P. Jiang, Y. Ramprakash, *Solid State Ionics* **1999**, *122*, 211.

[11] K. Sato, T. Misono, K. Murata, T. Fukui, H. Abe, M. Naito, *J. Eur. Ceram. Soc.* **2009**, *29*, 1119.

[12] S. Mosch, N. Trofimenko, M. Kusnezoff, T. Betz, M. Kellner, *Solid State Ionics* **2008**, *179*, 160.

[13] C. M. Grgicak, R. G. Green, W.-F. Du, J. B. Giorgi, *J. Am. Ceram. Soc.* **2005**, *88*, 3081.

[14] K. Sato, G. Okamoto, M. Naito, H. Abe, *J. Power Sources* **2009**, *193*, 185.

[15] M. Brown, S. Primdahl, M. Mogensen, *J. Electrochem. Soc.* **2000**, *147*, 475.

[16] X. Wang, N. Nakagawa, K. Kato, *J. Electrochem. Soc.* **2001**, *148*, A565.

[17] X. Wang, N. Nakagawa, K. Kato, *J. Electrochem. Soc.* **1999**, *146*, 2976.

[18] K. Sato, G. Okamoto, H. Abe, M. Naito, *ECS Trans.* **2007**, *7*, 1555.

[19] L. Xiang, X. Y. Deng, Y. Jin, *Scr. Mater.* **2002**, *47*, 219.

[20] S. Primdahl, Ph D thesis, Risø National Laboratory, Denmark **1999**.

[21] S. Primdahl, M. Mogensen, *J. Electrochem. Soc.* **1997**, *144*, 3409.

[22] S. Primdahl, M. Mogensen, *J. Electrochem. Soc.* **1998**, *145*, 2431.

[23] S. P. Jiang, S. Zhang, Y. D. Zhen, A. P. Koh, *Electrochem. Solid-State Lett.* **2004**, *7*, A282.

Dalton Transactions

View Online
Dynamic Article Links

Cite this: *Dalton Trans.*, 2011, **40**, 1073

www.rsc.org/dalton

PAPER

Surfactant-assisted one-pot synthesis of superparamagnetic magnetite nanoparticle clusters with tunable cluster size and magnetic field sensitivity†

Takanari Togashi,*[a] Takashi Naka,[b] Shunsuke Asahina,[c,d] Koichi Sato,[b] Seiichi Takami[d] and Tadafumi Adschiri*[a]

Received 24th September 2010, Accepted 25th November 2010
DOI: 10.1039/c0dt01280g

Magnetic nanoparticles (MNPs) have many potential biomedical applications. Improvements in their magnetic properties and solubility are necessary for these applications to realize their full potential. In this study, MNPs in the form of raspberry-like magnetite (Fe_3O_4) nanoparticle clusters, consisting of tiny Fe_3O_4 particles with a diameter of approximately 20 nm, were prepared under hydrothermal conditions at 200 °C in the presence of 3,4-dihydroxyhydroxysinnamic acid (DHCA). The primary particles were connected by DHCA molecules to form the clusters, which were well dispersed in water media because a COOH group from DHCA appeared on their surfaces. The cluster size could be tuned from 50 to 400 nm without changing the primary particle size by controlling the reaction time. Therefore, all prepared clusters displayed superparamagnetic properties at room temperature. In addition, the sensitivity of Fe_3O_4 to an external magnetic field could also be controlled by the cluster size.

Introduction

In recent years, many novel applications of magnetic nanoparticles (MNPs) have been proposed and investigated in the field of biological applications.[1] These include tags for sensing[2] and imaging,[3] drug delivery carriers,[4] hyperthermia for antitumor therapy,[5,6] magnetic resonance imaging (MRI) contrast agents,[7,8] and activity agents for medical diagnostics.[9,10] To use MNPs for biological applications, they should be well dispersed in water at a neutral pH region, and be covered with non-toxic molecules to avoid harm to humans. Therefore, the solubility of MNPs is also important for the biomedical field to disperse stably in water and deliver the MNPs at deceased parts, such as tumor cells, effectively; hence, superparamagnetism is one of the important properties of MNPs for use in biomedical applications.

Surface-modified Fe_3O_4 nanoparticles with organic molecules such as oleic acid and oleylamine, have been reported as a result of various reactions with surfactants.[11–14] On the other hand, magnetic properties of Fe_3O_4 particles for the applications mentioned above should be tuned approximately.

For magnetic manipulation and targeted delivery of Fe_3O_4 particles by using an external magnetic field, high magnetization is also required to effectively separate them from the suspension or to control their movement in blood. To obtain higher magnetization per particle, the particle size should be larger. However, when the particle size becomes larger, the particles are hardly dispersible in a solution because of a larger remnant magnetization, which might induce aggregation by an attractive force between MNPs even in the absence of a magnetic field. Therefore, it is difficult for magnetic materials for biological application to satisfy both appropriate magnetic property and high dispersibility. However, forming nanoparticle clusters which are formed by the connection of MNPs with some organic molecules or polymers is advantageous to control structural parameters, such as the interparticle distance and the cluster size, consequently, their magnetic properties and dispersibility.[15–18]

In this paper, we demonstrate a one-pot synthesis of water-dispersible raspberry-like Fe_3O_4 nanoparticle clusters with tunable diameter by hydrothermal synthesis using 3,4-dihydroxyhydroxycinnamic acid (DHCA; Scheme 1) as a modifier and interparticle linker.

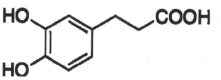

Scheme 1 Chemical structure of DHCA.

DHCA is one of the metabolites of L-phenylalanine and L-tyrosine and is found in fruits and vegetables.[19] Thus, it might be

[a]*Advanced Institute for Material Research, Tohoku University, 2-1-1 Katahira, Aoba-ku, Sendai, 980-8577, Japan. E-mail: togashi@tagen.tohoku.ac.jp; Fax: +81-22-217-5631; Tel: +81-22-217-5630*
[b]*National Institute for Material Science, 1-2-1 Sengen, Tsukuba, Ibaraki, 305-0047, Japan*
[c]*JEOL (EUROPE) SAS, Escape Claude Monet-1 All'ee de Civerny, 78290, France*
[d]*Institute for Multidisciplinary Research for Advanced Materials, Tohoku University, 2-1-1 Katahira, Aoba-ku, Sendai, 980-8577, Japan*
† Electronic supplementary information (ESI) available. See DOI: 10.1039/c0dt01280g

non-toxic to the human body. In addition, the DHCA molecule possesses a catechol group that has been well known as a strong anchor group for binding with various metal oxide surfaces.[20-22] Therefore, DHCA could be considered one of the best surfactant candidates for synthesizing biocompatible Fe_3O_4 nanomaterials.

The obtained clusters with a diameter of 50 to 400 nm were constructed of Fe_3O_4 nanoparticles with a diameter of approximately 20 nm. The magnetic response of a synthesized Fe_3O_4 nanocluster can be tuned by controlling the size of the nanocluster without the superparamagnetic–ferromagnetic transition; they could stably dissolve in water. All these properties are required for Fe_3O_4 particles intended for biomedical applications.

Experimental

Chemicals

Iron sulfate hexahydrate ($FeSO_4 \cdot 6H_2O$ 99%) and potassium hydroxide (KOH 99%) were purchased from Kojundo Chemical Laboratory Co., Ltd., and 3,4-dihydroxyhydroxycinnamic acid (DHCA 98%) was purchased from Sigma–Aldrich. These chemicals were used without further purification.

Synthesis

The reactant solution was prepared by mixing equal volumes of aqueous solutions of $FeSO_4$ (200 mM) and DHCA (400 mM), and then adjusting the pH of the solution to 9.5 by adding 5.0 M KOH solution dropwise. At this stage, the solution was dark red and contained no precipitate. Subsequently, 4.35 mL of the prepared solution were loaded into a pressure-resistant vessel (SUS316) with an inner volume of 5.0 mL. The reactor was capped tightly and heated in an electric furnace that was maintained at 250 °C for 10–120 min. The estimated pressure inside the reactor at 250 °C was 30 MPa. The reaction was terminated by cooling the reactor in a water bath at room temperature. The solid products were washed by three cycles of centrifugation, decantation, and redispersion into 10 mM of KOH aqueous solution. The collected particles were well dispersed in distilled water, and the aqueous solution was black.

Analysis

Powder X-ray diffraction (XRD) patterns were recorded on a Rigaku Ultima IV (Rigaku, Japan) in 2θ ranging from 20° to 80°. Transmission electron microscopy (TEM) was performed with a Hitachi H7650 (Hitachi, Japan) at 100 kV. All specimens for TEM were prepared by evaporating a diluted suspension on a carbon-coated copper grid. Field emission scanning electron microscopy (FESEM) was performed with a conventional objective lens at 1.0 kV. Fourier transformation infrared (FT-IR) spectra were obtained using an FT/IR680 (Jasco Co. Ltd., Japan). The spectra were recorded in the wavenumber range of 4000 to 600 cm^{-1}. Samples were ground and mixed with KBr and then pressed to form pellets. The background spectrum was obtained using pure KBr pellets as a standard. All zeta potential measurements were performed using a Zetasizer Nano ZS (Malvern Instruments Ltd, UK). The particles were suspended in water at a concentration of 0.1 wt% of Fe_3O_4. Subsequently, 0.01 M solutions of KOH and HCl were used to tune the pH of the aqueous solution between 10 and 3. Thermogravimetric analysis (TGA) measurements were performed on a TGDTA T8120 (Rigaku, Japan). All measurements were taken under a constant argon flow of 30 mL min^{-1}. The temperature was first kept at 105 °C for 30 min to remove most of the water, and then increased to 800 °C at a rate of 10 °C min^{-1}. The initial weight of each sample was approximately 5 mg. All the reported TGA curves were normalized with respect to the weight at 105 °C to ensure that only the solid fraction was measured.

Result and discussion

Characterization and crystal structure

The obtained particles were analyzed by XRD to identify the crystallographic structure. The peaks of all the samples can be identified as Fe_3O_4 (Fe_3O_4 JCPDS 86-1354) with lattice parameters of $a = 8.430$, 8.435, 8.428, 8.429, and 8.429 Å for reaction times of 10, 30, 60, 90, and 120 min, respectively, in good agreement with a previously reported value of $a = 8.432$ Å (Fig. 1).[23] In addition, the IR spectrum also supports this assignment (Fig. S1, ESI†). The sharp peak at 575 cm^{-1} seen in the IR spectrum is a characteristic peak of Fe_3O_4.[24] These results strongly support the identification of the products as Fe_3O_4. The crystallite sizes evaluated by Scherrer's equation were 20.1, 20.4, 21.6, 20.7, and 22.5 nm for reaction times of 10, 30, 60, 90, and 120 min, respectively. When the size of Fe_3O_4 particles decreases below 30 nm, the ferromagnetic–superparamagnetic transition occurs. Therefore, the synthesized Fe_3O_4 particles should be superparamagnetic.

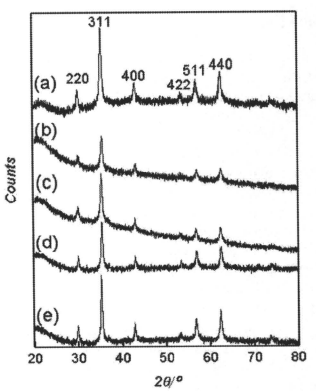

Fig. 1 XRD patterns of the products synthesized at 200 °C and 30 MPa for (a) 10, (b) 30, (c) 60, (d) 90, and (e) 120 min.

Fig. 2 shows TEM images of the magnetite particles. Particle size increased from 50 to 400 nm with increasing reaction time (Fig. 2(a)–(e)). However, the crystallite size evaluated by Scherrer's equation was smaller than that of the observed particles. In addition, the edges of the particles were rounded. These results imply that the observed particles are assembled structures of Fe_3O_4 nanoparticles. Lattice fringes were observed for a small cluster

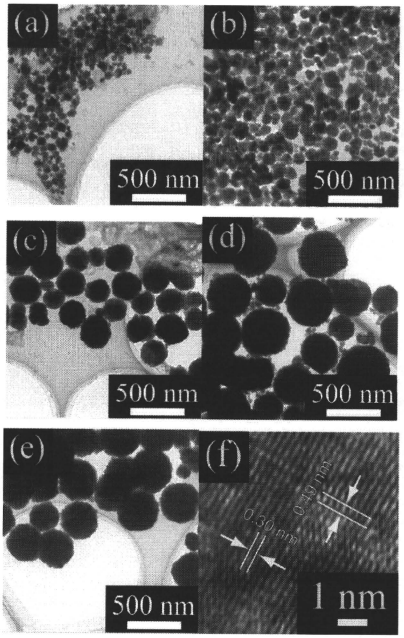

Fig. 2 TEM images of the synthesized Fe_3O_4 nanoclusters after reaction times of (a) 10, (b) 30, (c) 60, (d) 90, (e) 120 min, and (f) lattice image of the nanocluster with a reaction times of 30 min (whole HRTEM images are shown in the ESI†).

with a diameter of 100 nm, as shown in the high resolution TEM (HRTEM) image in Fig. 2(f). A clear lattice fringe can be seen in the HRTEM image, this indicates that the products have good crystallinity and were not amorphous. The measured distance between two adjacent planes in a specific direction gives a value of about 0.3 nm, which corresponds to the lattice spacing of 111 planes (0.487 nm) and 022 planes (0.297 nm), respectively, of magnetite. In addition The dark field image indicates that the products were not single crystal and composed tiny crystals (Fig. S2(b), ESI†), however a clear image of the whole structure of the products could not obtained (see ESI†).

To observe the whole structure of the nanoparticle cluster, those reacted for 120 min were observed by FESEM (Fig. 3). Fig. 3(a) shows a lower-magnification image. Tiny particles were assembled into structures with a raspberry-like morphology whose insides were filled. To confirm the crystal size of these particles, they were examined at a higher magnification (Fig. 3(d)). Tiny particles with a diameter of approximately 20 nm were observed at the surface of the larger particles. This size was almost the same as that of the crystallite evaluated by XRD peaks using Scherrer's equation.

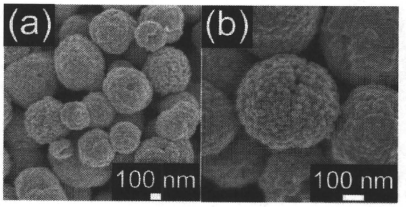

Fig. 3 FESEM images of the synthesized Fe_3O_4 nanoclusters after a reaction time of 120 min; (a) lower- and (b) higher-magnification images.

Surface properties of Fe_3O_4 clusters

The synthesized Fe_3O_4 surface was analyzed using FT-IR spectroscopy. In a typical IR spectrum, sharp peaks can clearly be seen at 1483 and 1258 cm^{-1} (Fig. 4). These peaks occur when catechol binds covalently to various metal oxides as catechol anions.[25,26] They were assigned to benzene ring vibration and a C–O stretch, respectively. Therefore, all catechol groups covalently bind to the Fe_3O_4 surface. Two peaks can be seen at 1630 and 1540 cm^{-1}; these were assigned to free COOH groups and those bound to Fe ions, respectively.[27,28] The peak at 1403 cm^{-1} was assigned as symmetric vibration of COO^- and COOH.[29] This indicates that all catechol groups, but not all COOH groups, bind to the Fe_3O_4 surface. This suggests two types of binding structures for the DHCA incorporated into the Fe_3O_4 nanoclusters (Scheme 2). Based on the SEM images and FT-IR spectra, we conclude that COOH groups at the outer surface do not bind to the Fe_3O_4 surface (Scheme 3).

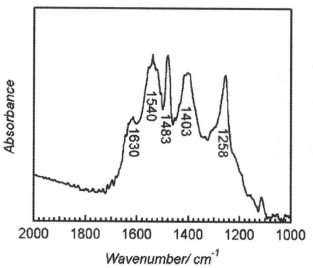

Fig. 4 Typical FT-IR spectrum of the synthesized Fe_3O_4 nanocluster after 120 min.

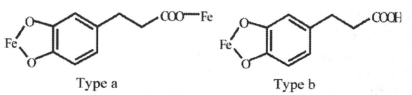

Scheme 2 Predicted structure of DHCA incorporated in Fe_3O_4 nanocluster.

To confirm the assumption described above, the chemical properties of the Fe_3O_4 surface were analyzed. The synthesized

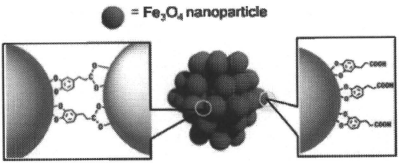

Scheme 3 Predicted structure of Fe_3O_4 nanocluster.

Fe_3O_4 nanoclusters dispersed well in water, possibly because the COOH groups were conjugated on the Fe_3O_4 surface. Macroscopic evidence indicates that DHCA is displayed on the surface of the Fe_3O_4 nanoclusters. In an alkaline aqueous solution (pH 10: Fig. 5(a)), the COOH groups were deprotonated and the Fe_3O_4 particles were well dispersed. The solution was stable for more than two months. In contrast, under acidic conditions (pH 2.0, Fig. 5(b)), the COOH groups were protonated and the raspberry-like Fe_3O_4 clusters precipitated within an hour, even without centrifugation. A similar result was reported by Tahir *et al.*[30] They synthesized a dopamine molecule with catechol and amino groups modified by TiO_2 nanorods that could be dispersed under acidic conditions (pH 2) but not in alkaline solution (pH 10).[31] This was possible because NH_2 could have a positive charge as a result of protonation. Our raspberry-like Fe_3O_4 nanoclusters were insoluble in acidic water, presumably because the COOH group on the surface was protonated and uncharged at pH 2.

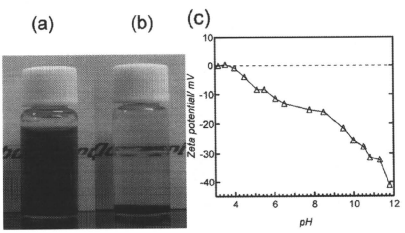

Fig. 5 Photographs of aqueous dispersions of Fe_3O_4 nanoclusters (1 wt%) at (a) pH 10 and (b) pH 2, and (c) zeta potential measurement of Fe_3O_4 for 200 nm.

Fig. 5(c) shows typical zeta potential measurements of raspberry-like Fe_3O_4 nanoclusters synthesized for 60 min; the value of the zeta potential increased gradually with decreasing pH. The zeta potential reached zero at pH 4.0, and positive values could not be shown. When the pH is lower than 4.2, DHCA becomes a neutral molecule by protonation of COOH groups.[32] The isoelectric point of the raspberry-like Fe_3O_4 nanoclusters (4.0) and the pK_a value of COOH groups of DHCA (4.2) were almost the same. This result strongly supports the suggestion that DHCA is immobilized with catechol groups, and COOH groups of DHCA are exposed on the surface of the raspberry-like Fe_3O_4 nanoclusters; hence, COOH groups do not bind to the surface of Fe_3O_4.

Previously, nanoparticle clusters have been prepared by using a polymer that would connect many nanoparticles by chemical interaction such as electrostatic interaction.[15–18] In our case, DHCA served as a glue for clusters. Therefore, this cluster formation using DHCA was different from the general cluster formation process using some polymers. The predicted Fe_3O_4 cluster formation and growth process is described below. The early state, in our case Fe_3O_4, was synthesized in the solution and the surface of the synthesized Fe_3O_4 nanoparticles was covered with catechol groups from DHCA, as in a previous report about *in situ* dopamine that also includes a catechol group modification method.[25,27]

Jia *et al.* reported the synthesis of Fe_3O_4 nanoparticles at the end of multiwalled carbon nanotubes (MCNTs).[32] Fe ions were concentrated at the end of the MCNTs, which were modified with COOH groups, and then Fe_3O_4 particles were synthesized around the region. Therefore, the Fe_3O_4 was generated only at the ends of the MCNTs. Also, in our case, the surface of the synthesized Fe_3O_4 was highly negatively charged by conjugated COOH groups, and thus it may follow a similar mechanism: Fe ions were concentrated on the surface and converted to tiny particles on the Fe_3O_4 surface. This process could be repeated to generate Fe_3O_4 nanoclusters (Scheme 4).

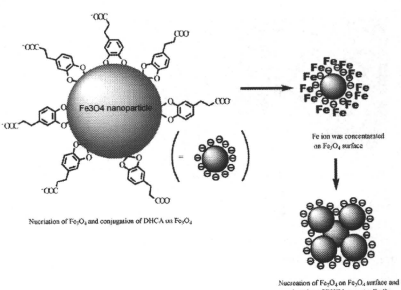

Scheme 4 Earlier stage of the predicted Fe_3O_4 nanocluster formation process.

To evaluate the coverage of the Fe_3O_4 surface by DHCA, TGA measurements were performed (Fig. 6). The decrease in the weight of the synthesized Fe_3O_4 clusters started at approximately

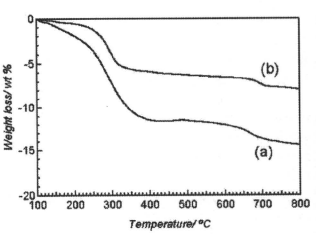

Fig. 6 Results of TGA measurements of Fe_3O_4 nanoclusters with diameters of (a) 50 and (b) 400 nm.

280 °C. This weight loss was caused by thermal decomposition of DHCA incorporated into the Fe_3O_4 cluster. The amount of organic molecules incorporated decreased from 14.4 to 7.9 wt% with increasing cluster size.

The predicted structure of the raspberry-like Fe_3O_4 nanoclusters (Scheme 3) suggests that there are two types of binding structure for DHCA in the nanoclusters: one in which DHCA binds two Fe_3O_4 nanoparticles on the nanocluster surface (type a in Scheme 2), and another in which it binds with one Fe_3O_4 nanoparticle on the nanocluster surface (type b in Scheme 2). As the cluster size grows, the molar ratio of type a DHCA becomes larger than that of type b DHCA. Type a DHCA covers two binding sites of primary Fe_3O_4; therefore, the relative amount of the organic molecules incorporated in Fe_3O_4 should decrease with increasing cluster size, consistent with the results above. In this study, the Fe_3O_4 content was approximately 85–90 wt%. This value was the highest amount of Fe_3O_4 in the synthesized nanoclusters; therefore, the prepared Fe_3O_4 clusters should have higher magnetization to an external magnetic field relative to Fe_3O_4 nanoparticles with a diameter of 20 nm.

Magnetic properties of the clusters

The magnetic properties of the raspberry-like Fe_3O_4 nanoclusters were measured using SQUID. Fig. 7(a) shows the magnetization–magnetic field (M–H) curves of the synthesized Fe_3O_4 nanoparticle clusters with diameters of 50 and 400 nm at 5 K. The saturation magnetization of Fe_3O_4 nanoclusters with diameters of 50 and 400 nm were 67.74 and 81.08 emu g^{-1}, respectively. To estimate the contribution of Fe_3O_4 particles in the nanoclusters, $M_{Fe_3O_4}$, were calculated using the equation described below:

$$M_{Fe_3O_4} = \frac{M_{observed}}{(W_{cluster} - W_{modifier})} \quad (1)$$

where $M_{observed}$, $W_{cluster}$, and $W_{modifier}$ are the observed saturation magnetization value of the Fe_3O_4 nanocluster with SQUID, the weight of the measured Fe_3O_4 nanoclusters, and the weight of the modifier included in the cluster as estimated by TGA measurement data, respectively. The saturation magnetic moment of pure Fe_3O_4 included in the nanoclusters with diameters of 50 and 400 nm were 79.14 and 88.03, respectively. The saturation magnetization increases with increasing cluster size. This tendency seems to be due to the surface disorder effect,[33] since the disorder in the individual nanocrystals was relieved by annealing. However, a more detailed analysis is required to clarify this dependence of magnetic properties on cluster size dependence of magnetic property. Fig. 7(b) shows a comparison of the hysteresis loop of the Fe_3O_4 nanocluster with a diameter of 400 nm at 5 and 290 K, respectively. At 290 K, remanence and coercivity could not be observed. This result suggests that the nanoparticle cluster with a diameter of 400 nm has superparamagnetic properties at room temperature. In contrast, a typical ferromagnetic hysteresis loop could be seen at 5 K, because thermal energy is insufficient to induce magnetic moment randomization, with a remnant magnetization M_r = 21.1 emu g^{-1} and coercivity H_c = 270 Oe, for comparison, M_r = 17.0 emu g^{-1} and H_c = 180 Oe at 5 K for the cluster with a diameter of 50 nm.

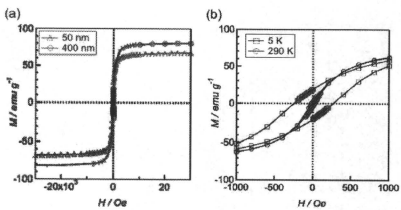

Fig. 7 Magnetic properties of the Fe_3O_4 nanoclusters measured at (a) 5 K (open triangle: 50 nm; open circle: 400 nm) and (b) comparison of hysteresis loop of Fe_3O_4 nanocluster with a diameter of 400 nm (open square: 5 K; open circle: 290 K).

Fig. 8 clearly demonstrates that magnetite nanoclusters with a diameter of 400 nm can be separated from the solution within minutes, while, smaller clusters (50 nm) could not be collected using a permanent magnet due to their small magnetization per particle. Note that this phenomena occurred under a magnetic field of ~3 kOe and the clusters were redispersed in water after a permanent magnet was removed (Fig. 8(c)). Magnetization of the Fe_3O_4 nanocrystals at the magnetic field of the permanent magnet H ~3 kOe is comparable for both clusters, as can be seen in Fig. 7(a). Plausibly, the sensitivity to an external magnetic field depends mainly on the size-dependent quantities in the hydrodynamics of magnetic colloidal suspension, such as fractional coefficient, diffusion constant,[34] and magnetization per cluster.

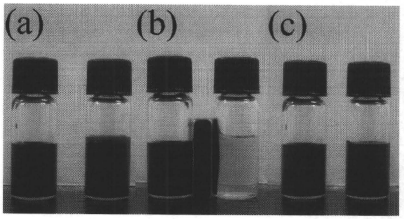

Fig. 8 Photographs of aqueous dispersions of Fe_3O_4 nanoclusters (1 wt%) in vials (a) without a magnetic field, (b) with a magnetic field for 1 min, and (c) after the magnetic field was removed. The size of Fe_3O_4 nanoclusters is 50 nm (left) and 400 nm (right).

The Fe_3O_4 clusters are soluble in water at concentrations up to 20 mg ml^{-1}. A highly concentrated Fe_3O_4 suspension behaved as a magnetic fluid. When the suspension was subjected to a strong magnetic field (3.5 kOe), it formed a crown-like morphology (Fig. 9). When the magnetic field was removed, the suspension reformed like a droplet, which is typical behaviour in a magnetic fluid. This high dispersibility of Fe_3O_4 nanoclusters would be important for use in biomedical applications.

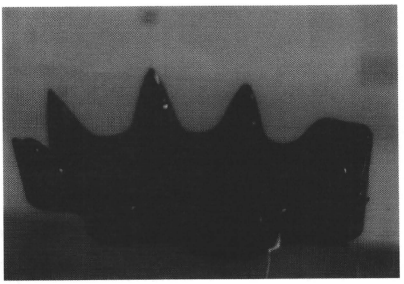

Fig. 9 Photograph of a concentrated aqueous dispersion (20 mg mL^{-1}) of a Fe_3O_4 nanocluster with a diameter of 200 nm above a permanent magnet (3.5 kOe).

Conclusions

In this study, we performed synthesis and cluster size tuning without changing the diameter of the primary particles with typical superparamagnetic properties. The average size of the clusters can be tuned from approximately 50 to 400 nm by controlling the reaction time. Nanostructured magnetic microspheres have many potential applications in the medical field, especially in diagnostics and drug targeting by magnetically guided transport. Another potential application is their use as actuators in small magnetomechanical devices. The obtained clusters could be dissolved in water at concentrations up to approximately 20 mg mL^{-1}, because large numbers of COOH groups were conjugated. In addition, the clusters could be manipulated by an external magnetic field because of their larger size and much higher magnetization per cluster. These properties are very important for biomedical applications because superparamagnetism enables high dispersibility of Fe_3O_4 in the liquid phase, and magnetite nanoclusters could be manipulated by an external magnetic field. This result would cause higher magnetization per cluster. In addition, DHCA, a non-toxic reagent, was used as a modifier; therefore, these clusters would be suitable for biomedical applications *in vivo*. Given that the surface of Fe_3O_4 was covered by COOH groups, biomolecules such as proteins and DNA, or drugs could be conjugated. Therefore, the prepared Fe_3O_4 clusters should be especially useful in the biomedical field as tags or carriers of magnetic manipulators.

Acknowledgements

This work was supported by a Grant-in-Aid for Scientific Research(S) (KAKENHI) No. 20226015.

Notes and references

1 S. Mornet, S. Vesseur, F. Grasset and E. Duget, *J. Mater. Chem.*, 2004, **14**, 2161.
2 J. M. Perez, F. J. Simeone, Y. Saeki, L. Josephson and R. Weissleder, *J. Am. Chem. Soc.*, 2003, **125**, 10192.
3 P. C. Wu, C. H. Su, F. Y. Cheng, J. C. Weng, J. H. Chen, T. L. Tsai, C. S. Yeh, W. C. Su, J. R. Hwu, Y. Tzeng and D. B. Shieh, *Bioconjugate Chem.*, 2008, **19**, 1972.
4 S. Kalele, R. Naranin and K. M. Krishnan, *J. Magn. Magn. Mater.*, 2009, **321**, 1377.
5 A. Jordan, P. Wust, H. Fähling, W. John, A. Hinz and R. Felix, *Int. J. Hyperthermia*, 1993, **9**, 51.
6 R. E. Rosensweig, *J. Magn. Magn. Mater.*, 2002, **252**, 370.
7 B. Bonnemain, *J. Drug Targeting*, 1998, **6**, 167.
8 Y. W. Jun, Y. M. Huh, J. S. Choi, J. H. Lee, H. T. Song, S. J. Kim, S. Yoon, K. S. Kim, J. S. Suh and J. Cheon, *J. Am. Chem. Soc.*, 2001, **127**, 5732.
9 J. H. Cho, S. G. Ko, K. C. Song and E. J. Choi, *J. Nanosci. Nanotechnol.*, 2009, **9**, 779.
10 J. M. Nam, C. S. Thaxton and D. A. Mirkin, *Science*, 2003, **301**, 1884.
11 S. Sun and H. Zeng, *J. Am. Chem. Soc.*, 2002, **124**, 8204.
12 F. Hu, Z. Zhou, Y. Ran, Z. Li and M. Gao, *Adv. Mater.*, 2006, **18**, 2553.
13 S. B. Wang, Y. L. Min and S. H. Yu, *J. Phys. Chem. C*, 2007, **111**, 3551.
14 S. Si. C. Li, X. Wang, D. Yu, Q. Peng and Y. Li, *Cryst. Growth. Des.*, 2007, **5**, 391.
15 J. Ge, Y. Hu, M. Biasini, W. P. Beyermann and Y. Yin, *Angew. Chem., Int. Ed.*, 2007, **46**, 4342.
16 T. Gong, D. Yang, J. Hu, W. Yang, C. Wang and Q. L. Lu, *Colloids Surf., A*, 2009, **339**, 232.
17 X. Liu, Y. Guan, Z. Ma and H. Liu, *Langmuir*, 2004, **20**, 10278.
18 A. Schilachter, M. E. Gruner, M. Spasova, M. Farle and P. Entel, *Phase Transitions*, 2005, **78**, 741.
19 S. Kim, S. Bok, S. Lee, H. Kim, M. Lee, Y. B. Park and M. Choi, *Toxicol. Appl. Pharmacol.*, 2005, **208**, 29.
20 M. Chanana, S. Jahn, R. Georgieva, J. Lutz, H. Bäumler and D. Wang, *Chem. Mater.*, 2009, **21**, 1906.
21 C. Xu, K. Xu, H. Gu, R. Zheng, H. Liu, X. Zhang, Z. Guo and B. Xu, *J. Am. Chem. Soc.*, 2004, **126**, 9938.
22 M. D. Shultz, J. U. Reveles, S. N. Khanna and E. E. Carpenter, *J. Am. Chem. Soc.*, 2007, **129**, 2482.
23 G. F. Goya, T. S. Berquó and F. C. Fonseca, *J. Appl. Phys.*, 2003, **94**, 3520.
24 R. M. Cornell, U. Schwertmann, in *Iron Oxides*, 2nd edn, 2003, pp. 146.
25 W. Huang, P. Jiang, C. Wei, D. Zhuang and J. L. Shi, *J. Mater. Res.*, 2008, **23**, 1946.
26 M. J. McWhirter, P. J. Bremer, I. L. Lamont and A. J. McQuillan, *Langmuir*, 2003, **19**, 3575.
27 T. Lana-Villarreal, A. Rodes, J. M. Pérez and R. A. Gómez, *J. Am. Chem. Soc.*, 2005, **127**, 12601.
28 D. H. Lee, R. A. Condrate and J. S. Reed, *J. Mater. Sci.*, 1996, **31**, 471.
29 K. Nakamoto, in *Infrared Spectra of Inorganic and Coordination Compounds*, 2nd edn, Wiley-Interscience, p. 223.
30 M. N. Tahir, P. Theato, P. Oberle, G. Melnyk, S. Faiss, U. Kolb, A. Janshoff, M. Stepputat and W. Tremel, *Langmuir*, 2006, **22**, 5209.
31 A. L. Petrou, P. Paraskevopoulou and M. Chrysikopoulou, *J. Inorg. Biochem.*, 2004, **98**, 123.
32 B. Jia and L. Gao, *J. Phys. Chem. B.*, 2007, **111**, 5337.
33 M. P. Morales, S. Veintemillas-Verdaguer, M. I. Montero and C. J. Serna, *Chem. Mater.*, 1999, **11**, 3058.
34 W. Hamley, *Introduction to Soft Mater*, John Wiley & Sons Ltd, 2007, West Sussex, England, p. 120, ch. 3.

Hybridisation of Sebacic Acid on the Surface of γ-Alumina Nanoparticles in Sub- and Supercritical Water

Varu Singh[a,b,c], Seiichi Takami[a,b], Kimitaka Minami[c], Daisuke Hojo[c], Toshihiko Arita[a,b], and Tadafumi Adschiri[a,b,c]

[a] Graduate School of Engineering, Tohoku University, 6-6 Aramaki Aza Aoba, Aoba-ku, Sendai 980-8579, Japan
[b] Institute of Multidisciplinary Research for Advanced Materials, Tohoku University, 2-1-1 Katahira, Aoba-ku, Sendai 980-8577, Japan
[c] World Premier International Research Center – Advanced Institute for Materials Research, Tohoku University, 2-1-1 Katahira, Aoba-ku, Sendai 980-8577, Japan

Reprint requests to Prof. T. Adschiri. E-mail: ajiri@tagen.tohoku.ac.jp

Z. Naturforsch. **2010**, *65b*, 1045 – 1050; received February 26, 2010

The surface modification of γ-alumina nanoparticles by sebacic acid in super- and subcritical water was investigated. The modified alumina was characterised by Fourier-transform infrared spectra, X-ray diffraction patterns, transmission electron microscopy images, and thermogravimetric studies. The alumina nanoparticles were found to remain stable, and sebacic acid was bound to their surfaces at 200 °C, but their crystallite structure was partially changed to that of boehmite above 200 °C. Under supercritical conditions at 400 °C, the alumina nanoparticles were totally changed to boehmite nanoparticles. The surface adsorption of sebacic acid is attributed to reactions between the surface -OH groups of alumina and the -COOH groups of sebacic acid. The modified alumina nanoparticles have -COOH groups on their surface, enabling hybridisation with various biomolecules, and thus allowing their application in several areas.

Key words: Surface Modification, Nano Alumina, Supercritical and Subcritical Water

Introduction

The chemical and physical properties of organic-inorganic hybrid nanocomposites are tailored by the association of organic and inorganic moieties at the nanometer scale. Organic molecule-modified inorganic particles show properties that are totally different from those of the original inorganic particles, making them widely applicable in areas such as electronics, magnetism, catalysis, and biology [1 – 5]. Various hybrid metal oxides and hydroxides have attracted much attention for their potential applications in industry and technology [6 – 8]. Alumina (Al_2O_3) is one of the most important oxides and has long been intensively studied because of its potential for broad application in adsorbents, catalysts, catalyst supports, and bioceramics [9 – 12]. Alumina is also used as filler to improve the properties of organic polymers, but for this purpose, it should disperse in these polymers by chemical bonding [13]. Alumina is also a typical candidate for biomaterials in bone and dental repair because of its hardness, chemical stability in living tissues and attractive tribological properties. For this purpose, biocompatibility of the alumina surface is important [14, 15]. Bertazzo *et al.* reported that a free carboxyl group can complex with the Ca^{2+} on the surface, forming sites of precipitation for calcium phosphate that make the alumina biocompatible [16]. Thus, there exists a need for development of the functionalisation of the alumina surface using chemically active functional groups.

Many researchers have investigated this topic and proposed different treatment techniques for capping the surface of nanoparticles to attach functional groups. In this paper, we report a simple hydrothermal method that allows to change the chemical properties of an alumina surface. In this method, the alumina surface is treated with a dicarboxylic acid for 15 minutes in subcritical water, which terminates the surface with carboxylic functional groups. These carboxylic groups enable hybridisation with polymers on the surface that makes nanoparticles biocompatible. However, as we show later in this paper, γ-alumina is not stable upon contact with water at higher temperatures because it transforms into a hydrated boehmite

0932–0776 / 10 / 0800–1045 $ 06.00

(AlOOH) phase. Therefore, suitable temperature conditions for modifying the alumina surface in water need to be achieved. Many studies have been conducted on boehmite nanoparticle synthesis and the stability of alumina [17, 18] because it is used in catalysis of several heterogeneous reactions. The present results can also be helpful in the studies of the thermal stability and transformation of alumina in super- and subcritical water.

Some researchers have also recently reported the use of dicarboxylic acids to modify the surface of nanoparticles to display -COOH groups. However, the reaction time required was quite long at lower temperatures [16]. Furthermore, some organic acids are not very soluble in water at room temperature, so lower temperatures are not suitable for surface modification with them. An advantage of the hydrothermal method is that sparingly water-soluble carboxylic acid can also be used for surface modification because the dielectric constant of water decreases at higher temperature to realise higher solubility of organic molecules.

In the work described in this paper, different temperature conditions (200 – 400 °C) were investigated in order to allow sebacic acid hybridisation on the surface of alumina nanoparticles in the water phase. The temperature was found to greatly affect both the stability of alumina and the sebacic acid adsorption on its surface.

Results and Discussion

XRD and TEM

Fig. 1a shows the X-ray diffraction (XRD) pattern of as-purchased alumina nanoparticles. All the peaks in the XRD pattern (Fig. 1a) agree with those of γ-alumina (Fig. 1d). Fig. 1b shows the XRD pattern of a sample treated with sebacic acid at 200 °C. This pattern shows only γ-alumina peaks without any other phase. The alumina nanoparticles clearly have maintained their shape under these conditions, as shown by the transmission electron microscopy (TEM) images in Figs. 2a and 2b. These results indicate that alumina particles are stable at this temperature.

Fig. 1c shows the XRD pattern of a sample processed at 400 °C. This XRD pattern is completely different from that of the as-purchased alumina nanoparticles (Fig. 1a). Clearly, the alumina particles are not stable, and a new crystalline phase was produced at 400 °C. All the peaks agree with those of boehmite (Fig. 1e), which is the hydrated phase of alumina. No additional peaks of phases other than boehmite were found, indicating that only well-crystallised boehmite nanoparticles have formed. Figs. 2c and 2d show TEM images of the orthorhombic morphology of the as-synthesised product processed with sebacic acid at 400 °C. The boehmite nanoparticles range in size from 10 nm to several hundred nanometres.

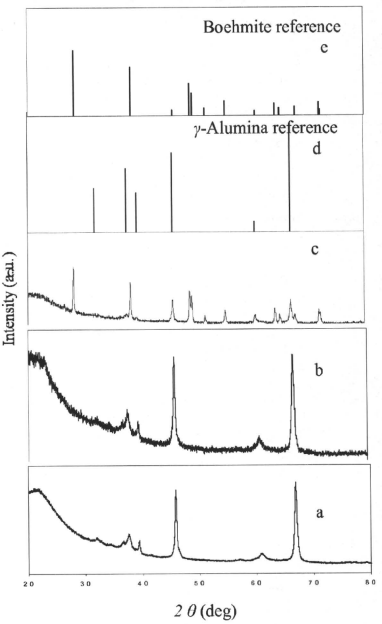

Fig. 1. XRD patterns of a) pure alumina nanoparticles, b) samples prepared with sebacic acid at 200 °C, c) at 400 °C, d) γ-alumina reference, and e) boehmite reference.

FTIR spectra

To investigate chemical bonding and the nature of the functional groups on the nanoparticle surfaces, Fourier-transform infrared (FTIR) analyses were conducted. Fig. 3a shows the FTIR spectrum of alumina nanoparticles treated with sebacic acid at 200 °C. At this temperature, the pure alumina phase was stable, and some new peaks appeared, possibly because of

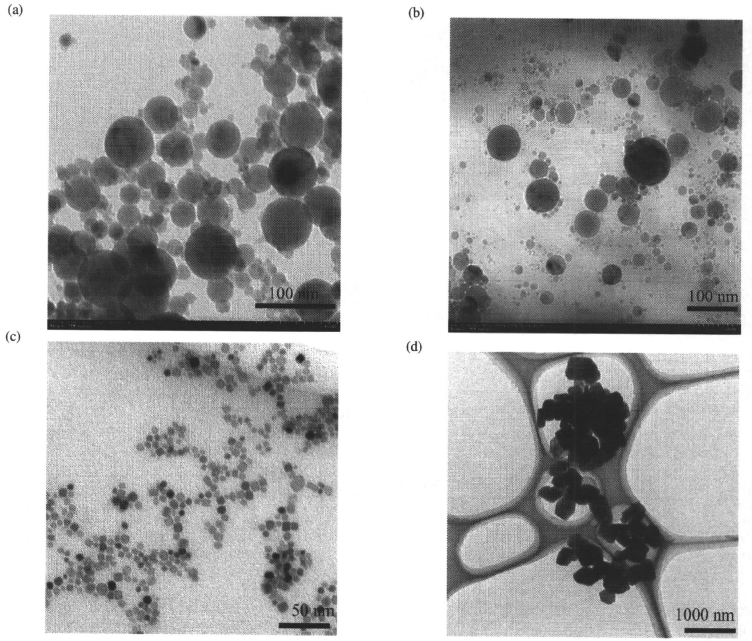

Fig. 2. TEM images of a) unmodified γ-alumina nanoparticles, as-prepared samples with sebacic acid, b) at 200 °C, and c), d) at 400 °C (boehmite nanoparticles).

adsorption of the sebacic acid modifier on the surface. A comparison of Figs. 3a and 3c shows that the nanoparticles treated with sebacic acid at 200 °C exhibit peaks characteristic of asymmetric and symmetric stretching of the methylene group -CH_2- at 2850 and 2931 cm^{-1}, respectively. These peaks were also observed in the FTIR spectrum of neat sebacic acid (Fig. 3d). The peaks at 1470 and 1580 cm^{-1} indicate the presence of -COO^- groups, and that at 1710 cm^{-1} indicates surface -COOH groups. The existence of -COOH and -COO^- groups suggests that one carboxyl group of sebacic acid is bound on the alumina surface while the one at the other end has remained unreacted.

On the other hand, when the particles were treated at 400 °C, boehmite was formed, as supported by the FTIR spectrum shown in Fig. 3b. The boehmite particles obtained at 400 °C show absorption bands at 1070, 1160, 1974, 2102, 3096, and 3299 cm^{-1}, which agree well with those reported in the literature [19]. These six bands can be ascribed to Al-OH stretching and bending vibrations in the boehmite structure. The two strong, well-separated absorption bands at 3096 and 3299 cm^{-1} indicate that the produced boehmite is highly crystalline [19]. All examinations confirm that the obtained product is the boehmite phase.

These results indicate that at 200 °C, hydration of alumina nanoparticles does not occur; therefore, this temperature is suitable for surface modification of alumina. At 400 °C, however, it is difficult to cap the surfaces of alumina nanoparticles with carboxylic acid because of their instability.

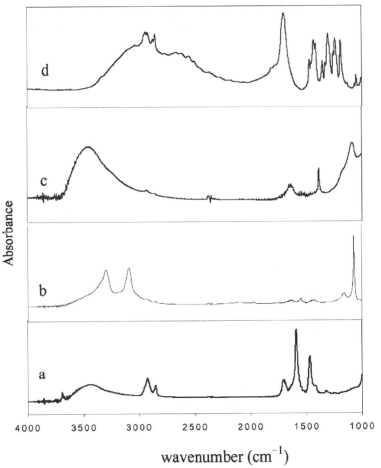

Fig. 3. FTIR spectra of as-prepared samples treated with sebacic acid at a) 200 °C, b) 400 °C, c) unmodified alumina particles, and d) sebacic acid.

Thermogravimetric analysis

To determine how much organic modifier is adsorbed on the surface of the treated nanoparticles, thermogravimetric (TG) measurements were carried out under a constant flow of Ar gas. The TG curve of pure alumina nanoparticles (Fig. 4a) shows a total of 1 % weight loss up to 800 °C. This may be due to free water on the nanoparticles. The TG curve for the alumina nanoparticles treated at 200 °C (Fig. 4b) shows that they lose about 2 % of their original weight up to 260 °C, which may correspond to crystalline water on their surfaces. After that, they lose about 17.3 % of their weight (Fig. 4b) from 280 to 625 °C. This weight loss corresponds to the loss of organic modifier from the surface of the alumina nanoparticles. Then, this curve (Fig. 4b) displays a plateau, indicating a stable phase. However, in the sample prepared at 400 °C (Fig. 4c), a drastic and sudden weight loss of 11.5 % occurrs from 485 to 550 °C, which is a higher temperature range than that shown by the curve in Fig. 4b. This weight loss corresponds to the dehydration of boehmite nanoparticles to form alumina nanoparticles. About 2 % weight loss was observed up to 480 °C,

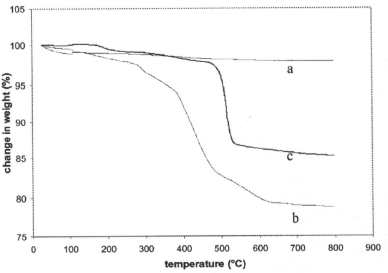

Fig. 4. Thermogravimetric analysis of a) pure alumina nanoparticles, b) alumina nanoparticles that were surface-modified at 200 °C, and c) boehmite nanoparticles obtained at 400 °C.

which corresponds to crystalline water and some modifier adsorbed on the surface of the boehmite nanoparticles.

This TG analysis has also clearly shown that the alumina nanoparticle surfaces were capped by sebacic acid at 200 °C, which was lost at comparatively low temperature. However, at 400 °C, the alumina changed to boehmite, and a major sharp weight loss was caused by dehydration of the boehmite particles.

Effect of reaction temperature

For the surface modification of alumina nanoparticles, the stability of alumina with the surface modifier under the experimental conditions is an important factor. To further examine the effect of the reaction temperature on the adsorption of sebacic acid on the surface of alumina nanoparticles, reactions were performed at 200, 280, 300, 350, 370, and 400 °C. XRD patterns and FTIR spectra of the particles processed at different temperatures are shown in Figs. 5 and 6, respectively. In broad terms, the results match those described above, indicating that γ-alumina particles were stable when processed at 200 °C and changed to boehmite particles as the temperature was increased from 200 to 400 °C (Fig. 5). This phase change may be associated with the chemical reaction of alumina with water at high temperature, because of which the γ-alumina particles dissolve in water. This dissolution is followed by subsequent precipitation of boehmite nanoparticles.

The boehmite particles obtained at 400 °C are well shaped and highly crystalline; thus, the crystal

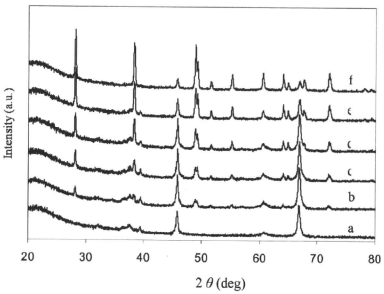

Fig. 5. XRD pattern of samples treated at a) 200 °C, b) 280 °C, c) 300 °C, d) 350 °C, e) 370 °C, and f) 400 °C.

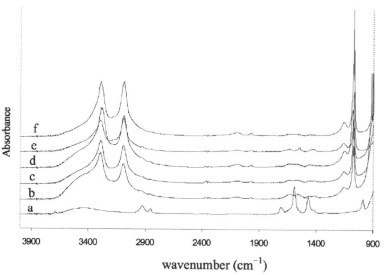

Fig. 6. FTIR spectra of samples treated at a) 200 °C, b) 280 °C, c) 300 °C, d) 350 °C, e) 370 °C, and f) 400 °C.

structure was completely changed from alumina to boehmite. As the temperature was increased from 200 to 400 °C, the intensity of the boehmite peaks in XRD (Fig. 5) and FTIR (Fig. 6) increased, and γ-alumina disappeared completely at 400 °C. When the particles were processed with a modifier at 280–370 °C, a mixture of γ-alumina and boehmite particles formed, as clearly shown in the XRD pattern (Fig. 5). However, in this temperature range, FTIR spectra do not show any modification of the surface of the γ-alumina particles, which may be due to dissolution of the reactive surface. Above 200 °C, free -OH was not observed; therefore, no surface modification occurred. As the temperature reached 400 °C, γ-alumina completely dissolved, and boehmite was formed. These results suggest that boehmite particles are produced by dissolution and reprecipitation. At higher temperatures, the chemical reaction of γ-alumina with water is expected to dissolve the alumina nanoparticles, and then recrystallisation is expected to give boehmite particles with the observed morphology. Fig. 7 illustrates the sub- and supercritical processes.

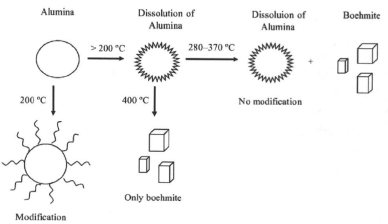

Fig. 7. Scheme of sub- and supercritical processes.

XRD results have indicated that alumina nanoparticles did not dissolve at 200 °C; therefore, free -OH groups on the alumina surface were available to react with -COOH. The intensity of the -OH peak of unmodified alumina at 3449 cm^{-1} (Fig. 3c) decreased after grafting, indicating that the hydroxyl groups were consumed and the concentration of the -OH groups on the alumina surface decreased. This shows that sebacic acid is adsorbed by a chemical reaction between -OH and -COOH. However, in the case of dicarboxylic acid, the reaction of both carboxylic groups of the dicarboxylic acid is also possible. This possibility can be minimised by using different chain lengths, concentrations and functional groups of the organic modifier.

Conclusion

The surface hybridisation of alumina nanoparticles with sebacic acid was investigated in super- and subcritical water conditions. Under supercritical conditions, alumina becomes unstable and is precipitated as orthorhombic boehmite nanoparticles, preventing adsorption of sebacic acid on the alumina surface. However, up to 200 °C, the carboxylic groups of sebacic acid modifiers can react with the hydroxyl groups on the surface of alumina nanoparticles. After modification, 17.3 % weight of the modifier is adsorbed on an alumina surface of 38 m^2 g^{-1}. Using this method with other organic modifiers, some functional groups such as -COOH and -NH_2 can be expected to appear on the surfaces of nanoparticles as active chemical functions.

Experimental Section

Materials and synthesis

All the reagents were analytically pure and used without further purification. Alumina nanoparticles were provided by Wako Chemicals, Ltd. The mean particle size was 20–200 nm, and their specific surface area was approximately 38 $m^2\ g^{-1}$. Sebacic acid [$HOOC(CH_2)_8COOH$], provided by Aldrich Chemicals, was used as an organic surface modifier. Ethyl alcohol and KOH were purchased from Wako Chemicals, Ltd. Deionised water was used to prepare the solutions. For surface modification of alumina nanoparticles, 0.020 g (0.20 mmol) of alumina nanoparticles and 0.120 g (0.59 mmol) of sebacic acid were loaded into a batch-type reactor with 5.0 mL internal volume. Then, 2.5 mL of 1.0 mM KOH solution, prepared in deionised water, was added. The pH of the reaction mixture is 5~6 at r. t. Next, the reactor was tightly capped and heated in an electric heater with continuous shaking at temperatures ranging from 200 to 400 °C for 15 min. Then, the reactor was submerged in cold water and cooled to r. t. The product was collected with ethyl alcohol and washed by four cycles of centrifugation-decantation using ethyl alcohol which is miscible with both water and sebacic acid.

Analysis

Before analyzing the products, the purified nanoparticles were dried under vacuum overnight. The products were characterised by an X-ray diffractometer (Rigaku) using CuK_α radiation in a 2θ-θ setup. The 2θ angle was scanned between 20 and 80°. The size and morphology of the particles were examined using TEM at an accelerating voltage of 100 kV. FTIR spectra were measured by a JASCO FT/IR-680 spectrometer; KBr was used for sample preparation because it is transparent to infrared radiation. A KBr pellet was prepared by grinding the solid sample with potassium bromide (KBr) and applying pressure to the dry mixture. TG analysis was performed with a Rigaku TAS-200 instrument in Ar atmosphere up to 800 °C.

[1] M. Ghosh, G. Lawes, A. Gayen, G. N. Subbanna, W. M. Reiff, M. A. Subramanian, A. P. Ramirez, J. Zhang, R. Seshadri, *Chem. Mater.* **2004**, *16*, 118–124.

[2] D. Rangappa, S. Ohara, M. Umetsu, T. Naka, T. Adschiri, *J. Supercrit. Fluid.* **2008**, *44*, 441–445.

[3] S. Takami, T. Sato, T. Mousavand, S. Ohara, M. Umetsu, T. Adschiri, *Mater. Lett.* **2007**, *61*, 4769–4772.

[4] B. D. Terris, T. Thomson, *J. Phys. D: Appl. Phys.* **2005**, *38*, R199.

[5] F. Bauer, U. Decker, H. Ernst, M. Findeisen, H. Langguth, R. Mehnert, V. Sauerland, R. Hinterwaldner, *Int. J. Adhes. Adhes.* **2006**, *26*, 567–570.

[6] K. Byrappa, S. Ohara, T. Adschiri, *Adv. Drug Deliver. Rev.* **2008**, *60*, 299–327.

[7] G. A. Somorjai, F. Tao, J. Y. Park, *Top. Catal.* **2008**, *47*, 1–14.

[8] N. Maximous, G. Nakhla, W. Wan, K. Wong, *J. Membrane Sci.* **2009**, *341*, 67–75.

[9] A. N. Tsvigunov, V. G. Khotin, V. V. Vaskevich, A. S. Krasikov, *Glass Ceram.* **2000**, *57*, 392–395.

[10] X. Huang, Z. Ma, Y. Wang, P. Jiang, Y. Yin, Z. Li, *J. Appl. Polym. Sci.* **2009**, *113*, 3577–3584.

[11] A. Khana, M. Riaz, S. B. Butt, J. H. Zaidi, *Sep. Purif. Technol.* **2007**, *55*, 396–399.

[12] Y. Zhu, H. A. Kishawy, *Int. J. Mach. Tool. Manu.* **2005**, *45*, 389–398.

[13] H. Li, Y. Yan, B. Liu, W. Chen, S. Chen, *Powder Technol.* **2007**, *178*, 203–207.

[14] Z. Qing, Z. Guang-Jie, D. H. L. Ng, Z. Xiao-Zhong, C. Zhi-Qing, *Biomaterials* **1999**, *20*, 595–599.

[15] L. Fernandez, G. Arranz, L. Palacio, C. Soria, M. Sanchez, G. Perez, A. E. Lozano, A. Hernandez, P. Pradanos, *J. Nanopart. Res.* **2009**, *11*, 341–354.

[16] S. Bertazzo, W. F. Zambuzzi, H. A. da Silva, C. V. Ferreira, C. A. Bertran, *Clin. Oral Implan. Res.* **2009**, *20*, 288–293.

[17] C. Xavier, M. Eric, L. Jean-François, C. Michel, *J. Colloid Interf. Sci.* **2007**, *308*, 429–437.

[18] T. Mousavand, S. Ohara, M. Umetsu, J. Zhang, S. Takami, T. Naka, T. Adschiri, *J. Supercrit. Fluid.* **2007**, *40*, 397–401.

[19] J. Zhang, F. Shi, J. Lin, S. Y. Wei, D. Chen, J. M. Gao, Z. Huang, X. X. Ding, C. Tang, *Mater. Res. Bull.* **2008**, *43*, 1709–1715.

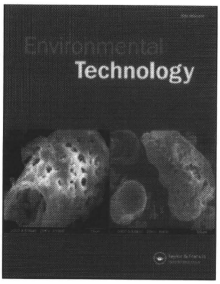

Environmental Technology
Publication details, including instructions for authors and subscription information:
http://www.informaworld.com/smpp/title~content=t791546829

In situ surface modification of molybdenum-doped organic-inorganic hybrid TiO_2 nanoparticles under hydrothermal conditions and treatment of pharmaceutical effluent

B. Shahmoradi[ab]; I. A. Ibrahim[c]; N. Sakamoto[d]; S. Ananda[e]; T.N. Guru Row[f]; Kohei Soga[g]; K. Byrappa[h]; S. Parsons[i]; Yoshihisa Shimizu[j]
[a] University of Mysore, Environmental Science Department, Karnataka 570009, India [b] School of Public Health, Faculty of Environmental Health Enginnering, Kermanshah University of Medical Science, Kermanshah, Iran [c] Central Metallurgical R&D Institute, Hellwan, Egypt [d] Shizuoka University, Hamamatsu-shi, Japan [e] Chemistry Department, University of Mysore, Karnataka 570009, India [f] Indian Institute of Science, Solid State and Structural Chemistry Unit, Bangalore 560012, India [g] Department of Materials Science and Technology, Tokyo University of Science, Chiba, Tokyo 278-8510, Japan [h] University of Mysore, Geology Department, Karnataka 570009, India [i] Cranfield University, Bedfordshire, United Kingdom [j] Research Center for Environmental Quality Management, Kyoto University, Otsu, Shiga 520-0811, Japan

Online publication date: 26 August 2010

To cite this Article Shahmoradi, B. , Ibrahim, I. A. , Sakamoto, N. , Ananda, S. , Guru Row, T.N. , Soga, Kohei , Byrappa, K. , Parsons, S. and Shimizu, Yoshihisa(2010) '*In situ* surface modification of molybdenum-doped organic-inorganic hybrid TiO_2 nanoparticles under hydrothermal conditions and treatment of pharmaceutical effluent', Environmental Technology, 31: 11, 1213 — 1220
To link to this Article: DOI: 10.1080/09593331003592261
URL: http://dx.doi.org/10.1080/09593331003592261